Paper number authorized by the organization committee

AI-Assisted Graph-Based Prediction of Debris Distribution from Periodic-Orbit Fragmentation in the Cislunar Region

Annika Anderson[1*], Sanghyeon Cho[2], Seur Gi Jo[1*], Hancheol Cho[2], David Canales[1]
[1] *Department of Aerospace Engineering, Embry-Riddle Aeronautical University, 1 Aerospace Boulevard, Daytona Beach, FL 32114, USA*
[2] *Department of Astronomy, Yonsei University, 50 Yonsei-Ro, Seodaemun-Gu, Seoul 03722, Republic of Korea*
* *Corresponding Author*

Abstract

The cislunar region has attracted increasing attention due to the growing number of planned missions. Its dynamics are governed by the combined gravitational influence of the Earth and Moon, leading to highly nonlinear and chaotic behavior. In this environment, collisions between spacecraft may generate debris fragments whose long-term evolution is difficult to predict and may disperse widely across the region. However, systematic tools for analyzing such fragmentation scenarios remain limited. This work extends a previously developed unified transport framework, in which braid-based symbolic dynamics derived from the universal template are generalized into a graph-based representation over the full cislunar domain. Within this framework, debris fragments are modeled as perturbed trajectories and classified into symbolic transport classes using the graph-based partition. This enables a compact symbolic and probabilistic description of debris outcomes. To reduce computational cost, a neural network-based surrogate model is introduced to learn the mapping between fragmentation conditions and outcome distributions. The trained model enables rapid prediction of debris behavior at arbitrary locations along a periodic orbit. The proposed approach provides an efficient and interpretable tool for debris risk assessment in the cislunar region.

Keywords: Cislunar, debris dispersion, graph-based modeling, neural network surrogate

1. Introduction

The cislunar region is rapidly emerging as a major arena of human space activity [1]. Unlike near-Earth space, the cislunar environment is governed by the combined gravitational influence of the Earth and Moon, producing highly nonlinear dynamics with sensitive dependence on initial conditions [2, 3]. Spacecraft fragmentation events in this regime can therefore generate debris populations whose long-term evolution is far harder to characterize than in geocentric orbits, and existing governance and tracking frameworks are not yet adequate to manage the resulting risks [4, 5]. Recent investigations have established preliminary benchmarks for cislunar fragmentation in dynamical models of varying fidelity, from the circular restricted three-body problem (CR3BP) to higher fidelity models [6–9]. Most of these studies sample fragments stochastically using the NASA Standard Breakup Model (SBM) [10–12], whose realization-dependent outputs are not naturally organized into the structured input-output pairs. As a result, systematic and learnable maps from breakup conditions to debris fate remain limited.

This work proposes a graph-based AI-assisted framework for predicting debris dispersion from a fragmentation near a periodic orbit. Rather than sampling fragments stochastically, an explosion is parametrized by its planar ejection direction and magnitude, producing a uniformly gridded $(\theta, \Delta v)$ space at each candidate breakup location along the parent orbit. This structured representation supports neural-network surrogate training and admits a direct orbital-mechanics interpretation: contiguous regions of the grid correspond to coherent transport channels. Each fragment trajectory is then classified using a graph-based partition of the cislunar configuration space, yielding a symbolic description of where the fragment ends up, which is used for neural-network surrogate training. The reference orbit is a planar distant retrograde orbit (DRO), which is well suited for sustained cislunar operations such as long-duration staging, logistics depots, and observational platforms, due to its inherent stability and low station-keeping requirements [7, 13]. For small Δv, the fragments are expected to remain near the parent orbit, providing a baseline against which the framework's classification of outcomes is benchmarked. The objectives of this work are to (**1**) construct a structured planar $(\theta, \Delta v)$ parametrization at multiple breakup locations along a stable cislunar reference orbit, (**2**) develop a graph-based symbolic classification of fragment final regions, (**3**) train a neural network surrogate to predict the final-region classification from the breakup state and ejection parameters, with the ability to generalize to previously unseen breakup locations, and (**4**) identify the primary drivers of class imbalance and surrogate prediction error, in order to inform targeted refinements in the final manuscript.

The paper is structured as follows. Section 2 develops the dynamical and fragmentation models. Then, Section 3 introduces the graph-based symbolic classification, with Section 4 presenting the surrogate representation. Finally, Section 5 concludes the paper revisiting each goal.

2. Dynamical Model and Problem Formulation

The Earth-Moon system is modeled in the planar CR3BP. The mass parameter is defined as $\mu = m_M/(m_E + m_M)$, with positions and time normalized by the Earth–Moon distance l^* and the characteristic period t^*, respectively. Considering a rotating frame in which the Earth and Moon are fixed at $(-\mu, 0)$ and $(1-\mu, 0)$, the equations of motion for a spacecraft of negligible mass are

$$\ddot{x} - 2\dot{y} = \frac{\partial U^*}{\partial x}, \qquad \ddot{y} + 2\dot{x} = \frac{\partial U^*}{\partial y}, \qquad \ddot{z} = \frac{\partial U^*}{\partial z}, \tag{1}$$

where the pseudo-potential is

$$U^* = \tfrac{1}{2}(x^2 + y^2) + \frac{1-\mu}{r_1} + \frac{\mu}{r_2}, \qquad r_1 = \sqrt{(x+\mu)^2 + y^2 + z^2}, \quad r_2 = \sqrt{(x-1+\mu)^2 + y^2 + z^2}. \tag{2}$$

Note that five equilibrium points emerge from Eq. (1): three collinear, dynamically unstable points L_1, L_2, L_3 along the Earth–Moon line, and two linearly stable equilateral points L_4, L_5. These partition the position space into qualitatively distinct dynamical regimes, motivating the symbolic regions used in Section 3. The parent orbit is a planar DRO with period $T_{\text{DRO}} \approx 2.43$ days; under small velocity perturbations, fragments are expected to remain near the parent orbit, providing a controlled test case for evaluating the framework's classification of escape, transit, and Moon-impact outcomes.

2.1. Fragmentation Modeling near Periodic Orbits

Fragment populations are generated by applying a planar velocity perturbation to a nominal state on the parent DRO (Fig. 1). The breakup is assumed instantaneous, so fragment positions are unchanged and the perturbation is applied entirely to the velocity. For an initial state $\vec{x}_0(t_k) = [x_0, y_0, \dot{x}_0, \dot{y}_0]^\top$ at the k-th breakup location ($k = 1 - 199$), each fragment initial condition takes the form

$$\vec{x}_{0,\text{frag}}(\theta, \Delta v;\, t_k) = \vec{x}_0(t_k) + \big[\,0,\ 0,\ \Delta v\cos\theta,\ \Delta v\sin\theta\,\big]^\top, \tag{3}$$

where $\theta \in [0°, 360°)$ is the ejection direction measured from the $\hat{x}$-axis, and $\Delta v \in [0, 500]$ m/s is the ejection magnitude. The grid is uniform: θ in 5° increments and Δv in 5 m/s increments, producing $73 \times 101 = 7{,}373$ fragments per breakup location.

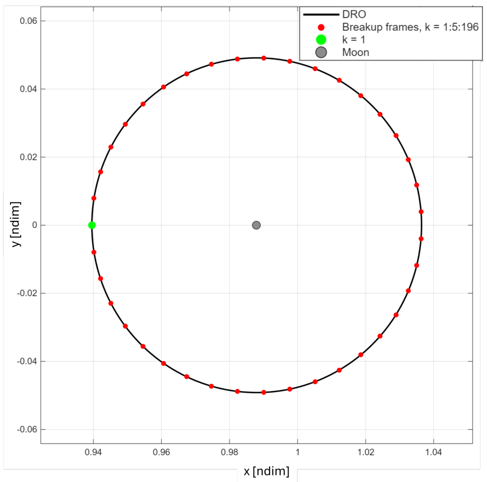

Fig. 1. Planar DRO used as the parent orbit for the fragmentation analysis

Although the SBM [10–12] is widely used to model realistic fragment populations in fragmentation studies, this work replaces it with a structured grid representation. This choice yields a tensorized set of inputs and outcomes that is significantly more amenable to neural-network surrogate training than a stochastic ensemble. It also preserves a clear orbital-mechanics interpretation: the $(\theta, \Delta v)$ parametrization at each breakup location directly encodes ejection geometry, and contiguous regions of the grid correspond to coherent transport channels as seen in the next section.

3. Graph-Based Symbolic Classification of Debris Outcomes

To provide a compact and interpretable representation of debris trajectories, a graph-based symbolic framework is adopted, extending braid-based symbolic dynamics derived from the universal template to a global representation over the cislunar domain [3, 14]. The cislunar region is divided into a finite set of regions $\mathcal{R} = \{R_1, R_2, \ldots, R_N\}$ defined by the geometry of the gravitational potential field. Adjacency between regions defines a directed graph in which nodes represent spatial regions and edges represent admissible transitions under the flow. The collinear points L_1 and L_2 form saddle regions acting as transport gateways, while the triangular points L_3, L_4, L_5 define a ridge separating qualitatively distinct trajectory behaviors. Motivated by this structure, circular boundaries are introduced around L_1 and L_2 with radii $r_{L_1} = 0.2740$ and $r_{L_2} = 0.3790$ (ndim) based on the isolating block condition [3, 14–16], and an outer boundary approximating the L_3–L_4–L_5 ridge separates the exterior region. Each region is assigned a numerical label that encodes its location: values in the 10s correspond to the lunar, L_1, and L_2 gateway regions, those in the 20s to the Earth-vicinity region, and those in the 30s to the exterior region. A detailed description of the $\mathcal{R}$ is provided in Appendix A.

A debris fragment trajectory $\vec{x}(t)$ is encoded as a symbolic sequence

$$\mathcal{B} = \{b(\vec{x}(t_1)) - b(\vec{x}(t_2)) - \cdots - b(\vec{x}(t_f))\}, \tag{4}$$

with $b(\vec{x}(t_k)) = R_i$ if $\vec{x}(t_k) \in R_i$, converting a continuous trajectory into a discrete sequence of region transitions. For example, a nominal DRO trajectory is represented by a repeating symbolic pattern such as $\mathcal{B} = 12 - 13 - 14 - 13 - 12$, reflecting its periodic transport structure within the lunar region. The full sequence captures the trajectory's transport history, but for surrogate training, only the final symbol $b(\vec{x}(t_f))$ is retained as the prediction target, summarizing each fragment by where it ends up after the propagation horizon. Fig. 2 shows the resulting final-region maps over the $(\theta, \Delta v)$ grid for six breakup locations along the parent DRO propagated for 5 nondimensional time units. The dominant coherent-cell structure is preserved across the orbit, while cell areas and the prevalence of individual labels shift substantially with breakup location, indicating that the location index itself carries information for the surrogate.

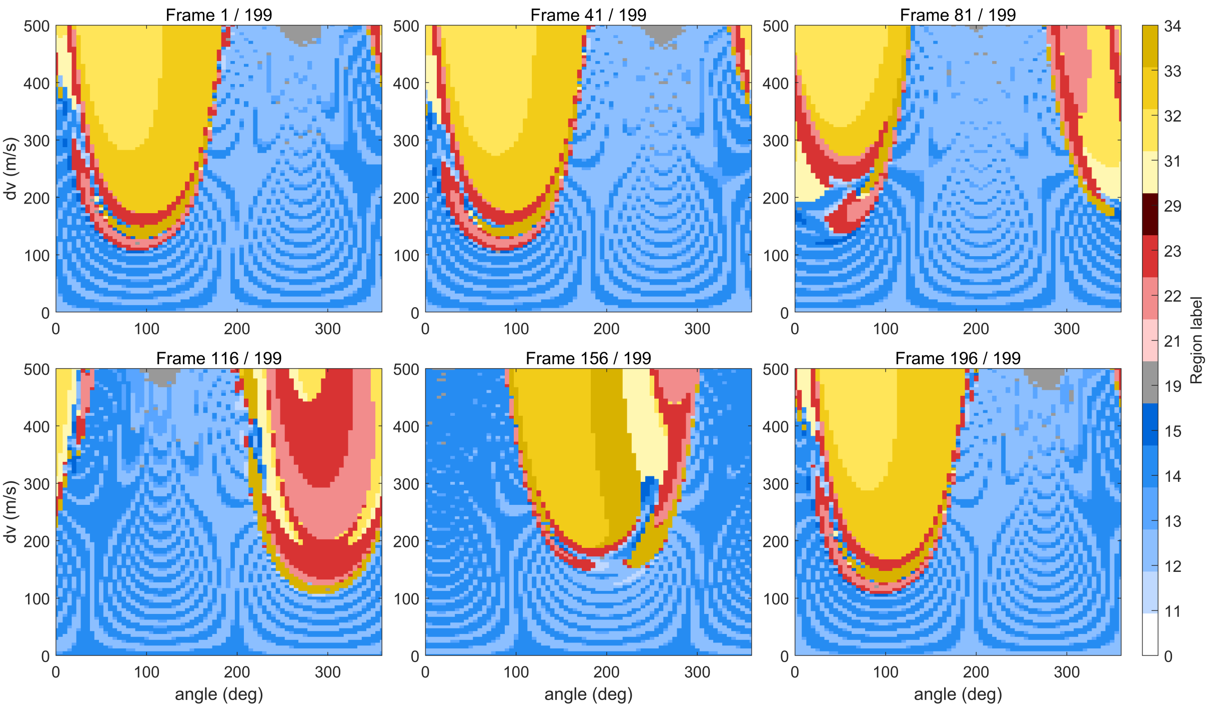

Fig. 2. Final-region maps for six breakup locations along the parent DRO. Region labels are read directly from the colorbar (10s: Moon vicinity, 20s: Earth-side, 30s: exterior; 19 denotes Moon impact).

4. AI-Based Prediction of Debris Distribution

To predict the final-region label without repeated CR3BP propagation, a neural-network surrogate is formulated as a multi-class classification problem. The input consists of the breakup state along the DRO and the velocity perturbation parameters,

$$[x, y, \dot{x}, \dot{y}, \sin\theta, \cos\theta, \Delta v],$$

and the output is the graph-based symbolic region label after 5 nondimensional time units. To test generalization to unseen breakup locations, the data are split by the spatial index k (every fifth index up to $k = 196$), with 26 locations for training, 6 for validation, and 8 for testing. A multilayer perceptron (MLP) is used as the classifier. The input features are standardized using the training-set mean and standard deviation, and the model is trained with the Adam optimizer and cross-entropy loss.

Table 1 compares several settings, including class-weighted loss, larger MLP architectures, and feature engineering with radial distance, radial/tangential velocity, Δv components, and post-breakup velocity. Feature engineering alone does not improve the performance; both the overall accuracy and balanced accuracy decrease compared with the basic baseline. In contrast, class weighting lowers the overall accuracy but improves balanced accuracy, indicating less bias toward majority labels. When class weighting and feature engineering are used together, increasing the model size gives only modest additional improvement in balanced accuracy. Overall, the results show that the model captures the dominant final-region structure, although narrow or boundary-like labels remain difficult to recover. This trend is also visible in Fig. 3, where the large MLP model reproduces the dominant final-region structure for $k = 151$, while errors remain concentrated near fine boundaries.

Future work will focus on imbalance-aware training, feature refinement, and more expressive architectures to improve rare and boundary-like label prediction.

Table 1. Comparison of MLP classification performance under different training settings.

Model	Hidden dims.	Acc	Bal. Acc	Option
Baseline	128–128–64	0.730	0.628	Basic
Baseline	128–128–64	0.678	0.742	Class weight
Baseline	128–128–64	0.725	0.609	Feature engineering
Baseline	128–128–64	0.678	0.734	Class weight + feature engineering
Medium	256–256–128	0.697	0.748	Class weight + feature engineering
Medium–deep	256–256–128–64	0.693	0.761	Class weight + feature engineering
Wide	512–256–128	0.698	0.758	Class weight + feature engineering
Large	1024–1024–512–256	0.701	0.759	Class weight + feature engineering

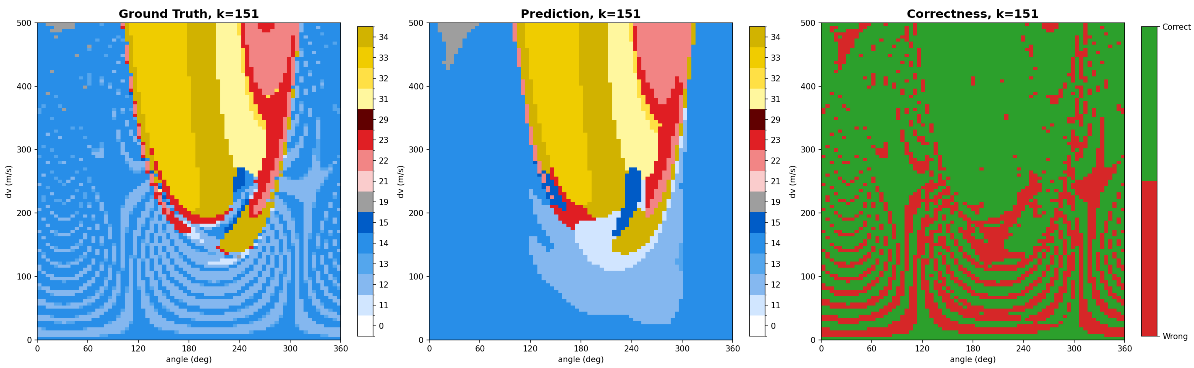

Fig. 3. Comparison of the ground-truth labels (left), predicted labels (middle), and prediction correctness (right) for $k = 151$ using the large MLP model.

5. Conclusions

This work introduces a structured, graph-based, and AI-assisted framework for predicting debris dispersion from a fragmentation near a planar DRO. A uniform $(\theta, \Delta v)$ grid samples 40 breakup locations along the parent orbit; the resulting fragments are propagated under planar CR3BP dynamics and classified using a graph-based partition of the cislunar region. A multilayer perceptron trained on this dataset reproduces the dominant final-region structure on unseen breakup locations, with overall accuracy of 73.0% for the baseline and balanced accuracy reaching as high as 76.1% once class weighting and a deeper architecture are applied (Table 1). The accuracy/balanced-accuracy trade-off observed across the training settings localizes the error to boundary-like Moon-vicinity labels rather than to dominant flows.

Returning to the goals of Section 1: the structured $(\theta, \Delta v)$ parametrization (**1**) produces informative coherent structures and final-region maps; the graph-based classification (**2**) compresses each trajectory to an interpretable symbolic label; the surrogate (**3**) generalizes to unseen breakup locations at usable accuracy; and the imbalance signature (**4**) is localized to specific narrow labels, identifying where additional training-data and architectural attention is required. Future work will pursue more aggressive imbalance-aware training and architectural variants and evaluate the trained surrogate on the remaining DRO indices; extension to other cislunar periodic orbits is another natural next step.

Acknowledgements

This work is supported by the National Science Foundation under ERI Award CMMI-2501408 (PI: Dr. David Canales). The authors also acknowledge the support of the Space Trajectories and Applications Research (STAR) group at Embry-Riddle Aeronautical University.

Appendix A: Definition of the Graph-Based Partition in the Cislunar Region

This appendix defines the graph-based partition of the cislunar region (Fig. 4). Each region label R_i is referred to as a *braid word*, denoted by $b(\vec{x})$, representing a symbolic element derived from braid-based dynamics, which encodes the spacecraft state according to its location within the partitioned cislunar domain. Let (x, y, z) denote the spacecraft position in the rotating barycentric frame, and μ the Earth–Moon mass parameter, R_E and R_M the radii of the Earth and Moon, respectively, and L_i the position of the i-th libration point. The auxiliary distances are defined as

$$d_E = \sqrt{(x+\mu)^2 + y^2}, \qquad d_M = \sqrt{(x-1+\mu)^2 + y^2}, \qquad d_G = \sqrt{(x-h)^2 + y^2}, \tag{5}$$

where d_E and d_M are used to denote planar distances consistent with the graph-based partition, which is defined in the (x, y) plane, and d_G denotes the distance from the center of the graph partition boundary. The large circle has center $(h, 0)$ and radius a. Isolating block boundary near L_1 and L_2 are denoted by $r_L = 0.2740$ and $r_R = 0.3790$, respectively. The braid word assignment is defined piecewise according to the following conditions:

$$b(\vec{x}) = \begin{cases} 11, & d_M \le r_L,\ x < x_{L_1}, \\ 12, & \big((d_G \le a \text{ and } d_M \le r_L) \ \text{ or } \ (d_G > a \text{ and } d_M \le r_R)\big),\ x_{L_1} \le x < 1-\mu-R_M, \\ 13, & d_M \le r_R,\ 1-\mu-R_M \le x \le 1-\mu+R_M, \\ 14, & d_M \le r_R,\ x > 1-\mu+R_M, \\ 15, & d_M \le r_R,\ x \ge x_{L_2}, \\ 19, & d_M \le R_M, \\ 21, & d_G \le a,\ d_M > r_L,\ x < -\mu-R_E, \\ 22, & d_G \le a,\ d_M > r_L,\ -\mu-R_E \le x \le -\mu+R_E, \\ 23, & d_G \le a,\ d_M > r_L,\ x > -\mu+R_E, \\ 29, & d_E \le R_E, \\ 31, & d_G > a,\ d_M > r_R,\ x \ge x_{L_4},\ y \ge 0, \\ 32, & d_G > a,\ d_M > r_R,\ x < x_{L_4},\ y \ge 0, \\ 33, & d_G > a,\ d_M > r_R,\ x < x_{L_4},\ y < 0, \\ 34, & d_G > a,\ d_M > r_R,\ x \ge x_{L_4},\ y < 0. \end{cases} \tag{6}$$

Note that the labels 19 and 29 denote Moon impact and Earth impact, respectively. A trajectory generates a *braid class* by concatenating the sequence of braid words encountered along its time evolution, providing a symbolic representation of its transport behavior.

References

[1] Baker-McEvilly, B., Bhadauria, S., Canales, D., and Frueh, C., "A comprehensive review on Cislunar expansion and space domain awareness," *Progress in Aerospace Sciences*, Vol. 147, 2024, pp. 101019.

[2] Canales, D. and Howell, K., "Understanding Flow around Planetary Moons via Finite-Time Lyapunov Exponent Maps," *Celestial Mechanics and Dynamical Astronomy*, Vol. 136, 09 2024.

[3] Jo, S. G., Canales, D., and Howell, K. C., "Understanding Chaotic Motion in the Cislunar Region with Ghrist's Universal Template," *Proceedings of the 76th International Astronautical Congress (IAC)*, Sydney, Australia, October 2025.

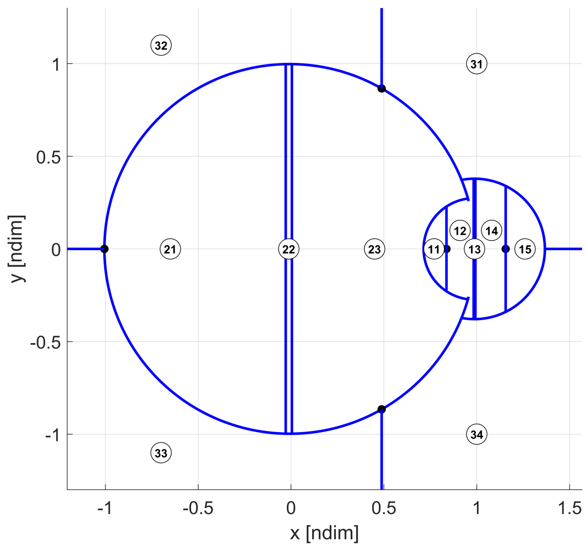

Fig. 4. Graph-based partition of the cislunar region.

[4] Chhabra, A., Sinha, A., Weeden, B., and Beeson, R., "Addressing gaps in cislunar orbital debris mitigation governance frameworks via norms of behavior," *Space Policy*, 2025, pp. 101724.

[5] Barakat, B. F. and Kezirian, M. T., "Establishing requirements for lunar and cislunar orbital debris tracking," *Journal of Space Safety Engineering*, Vol. 11, No. 3, 2024, pp. 446–453.

[6] Guardabasso, P., Skoulidou, D. K., Bucci, L., Letizia, F., Lemmens, S., Ansart, M., Roser, X., Lizy-Destrez, S., and Casalis, G., "Analysis of accidental spacecraft break-up events in cislunar space," *Advances in Space Research*, Vol. 72, No. 5, 2023, pp. 1550–1569.

[7] Boone, N. R., Bettinger, R. A., and Little, B. D., "Simulation of Debris Events in Cislunar Orbits Near the Moon," *Journal of Spacecraft and Rockets*, Vol. 62, No. 6, 2025, pp. 2030–2046.

[8] Black, A. and Frueh, C., "Fragmentation characterization in the circular restricted three body problem for cislunar space domain awareness," *Advances in Space Research*, Vol. 75, No. 1, 2025, pp. 1177–1204.

[9] Anderson, A., Sanaga, R. R., Girard, A., and Canales, D., "Intermediate-Fidelity Modeling of Debris Hazards in the Earth-Moon System for Upcoming Cislunar Missions," *AIAA Ascend Washington D.C.*, 05 2026.

[10] Liou, J.-C. and Johnson, N. L., "NASA Standard Breakup Model, Orbital Debris Engineering Model 3.1 User's Guide," 2006, NASA Orbital Debris Program Office.

[11] Johnson, N. L., Krisko, P. H., Liou, J.-C., and Anz-Meador, P. D., "NASA's new breakup model of EVOLVE 4.0," *Advances in Space Research*, Vol. 28, No. 9, 2001, pp. 1377–1384.

[12] Black, A. A., *Decluttering the cosmos: characterizing fragmentation behaviour in cislunar and near earth environments for space domain awareness*, Ph.D. thesis, Purdue University, 2024.

[13] Bezrouk, C. and Parker, J. S., "Long term evolution of distant retrograde orbits in the Earth-Moon system," *Astrophysics and Space Science*, Vol. 362, No. 9, 2017, pp. 176.

[14] Jo, S. G. and Canales, D., "Lagrangian Coherent Structure–Based Trajectory Grouping and Dynamic Mode Decomposition Surrogates for Cislunar Chaos Control," *5th International Conference on Space Situational Awareness*, 04 2026.

[15] Jo, S. G., Canales, D., and Howell, K., "Introducing Ghrist's Universal Templates and Isolating Blocks to Categorize Motion through the L2 Earth-Moon Gateway," *2025 AAS/AIAA Space Flight Mechanics Meeting*, 01 2025.

[16] Schmitt, J., Jo, S. G., Torrente, M., Arnold, H., Aros, M., Chaparro, B. S., Howell, K. C., and Canales, D., "Interpreting High-Dimensional Earth–Moon Space Mission Design with Supervised Learning and Augmented Reality," *2026 IEEE International Conference on Artificial Intelligence and eXtended and Virtual Reality (AIxVR)*, Osaka, Japan, 2026.